Journal of Power Sources 339 (2017) 51–60

Contents lists available at ScienceDirect

Journal of Power Sources

journal homepage: www.elsevier.com/locate/jpowsour

Stabilization of organometal halide perovskite films by SnO_2 coating with inactive surface hydroxyl groups on ZnO nanorods

Peng Wang [a], Jinjin Zhao [a, b, d, *], Jinxi Liu [c], Liyu Wei [a], Zhenghao Liu [a], Lihao Guan [a], Guozhong Cao [b, **]

[a] School of Materials Science and Engineering, Shijiazhuang Tiedao University, 17 Northeast, Second Inner Ring, Shijiazhuang, 050043, China
[b] Department of Materials Science and Engineering, University of Washington, Seattle, WA, 98195-2120, USA
[c] Department of Engineering Mechanics, Shijiazhuang Tiedao University, 17 Northeast, Second Inner Ring, Shijiazhuang, 050043, China
[d] Shenzhen Key Laboratory of Nanobiomechanics, Shenzhen Institutes of Advanced Technology, Chinese Academy of Sciences, Shenzhen, 518055, China

HIGHLIGHTS

- Core-shell ZnO@SnO_2 NRs were fabricated by depositing SnO_2 layer on the ZnO NRs.
- The efficiency was increased from 6.92% to 12.17% by applying SnO_2 passivation.
- The SnO_2 passivation layer effectively suppresses the degradation of perovskite.
- The introduction of SnO_2 much enhanced thermal stability of perovskite films.

GRAPHICAL ABSTRACT

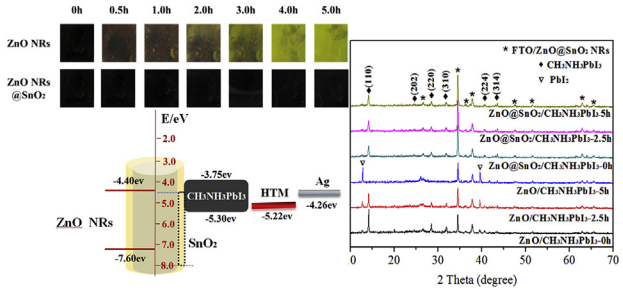

ARTICLE INFO

Article history:
Received 8 September 2016
Received in revised form
15 October 2016
Accepted 11 November 2016
Available online 18 November 2016

Keywords:
Perovskite solar cell
Surface passivation
Thermal and chemical stability
$CH_3NH_3PbI_3$
ZnO and SnO_2 core-shell arrays

ABSTRACT

Perovskite solar cells have advanced rapid in the last few years, however the thermal instability of perovskite film on ZnO nanorods (NRs) remains a big challenge limiting its commercialization. The present work demonstrated effective suppression of the decomposition of $CH_3NH_3PbI_3$ perovskite through inserting a thin tin oxide (SnO_2) passivation layer between ZnO NRs and perovskite films. Although X-ray photoelectron spectroscopy (XPS) results showed no distinct difference in the amount of hydroxyl groups and oxygen vacancies on the surface of ZnO NRs and ZnO@SnO_2 NRs, Raman spectra suggested the hydroxyl groups might be trapped in oxygen vacancies on SnO_2 surface, preventing the decomposition of $CH_3NH_3PbI_3$ perovskite through reacting with the hydroxyl groups. The power conversion efficiency of perovskite solar cells was significantly increased from 6.92% to 12.17% and became hysteresis-free by applying SnO_2 passivating layer between perovskite and ZnO layers.

1. Introduction

Organometal halide perovskite solar cells (PSCs) have attracted much attention due to their power conversion efficiency (PCE) up to 22% [1–13]. In a typical solar cell device, a mesoporous TiO_2 film is commonly used as an electron transporting layer (ETL); however, it has a low electron mobility (0.1–4 cm^2/Vs) [14,15], and control of

* Corresponding author. School of Materials Science and Engineering, Shijiazhuang Tiedao University, 17 Northeast, Second Inner Ring, Shijiazhuang, 050043, China.
** Corresponding author.
E-mail addresses: jinjinzhao2012@163.com (J. Zhao), gzcao@u.washington.edu (G. Cao).

http://dx.doi.org/10.1016/j.jpowsour.2016.11.046
0378-7753/

its morphology and crystallinity requires complex and multistep processes including high temperature annealing [16–19]. ZnO crystallizes relatively easily in most solution processes with a variety of morphologies readily attainable and crystalline ZnO possesses high electron mobility of 110–138 cm^2/V s, several orders of magnitude higher than that of TiO_2 [20–27].

ZnO has been used as an electron transporting layer in PSCs, mostly with ZnO nanoparticles or nanorods [28–34]. ZnO nanoparticles suffer from relatively slow electron transport and high charge recombination because of the presence of many grain boundaries and surface defects [29,35]. Single crystalline ZnO nanorods offer an easy path for charge transfer due to the absence of grain boundaries and the presence of an internal electric field along the c-axis, also the common nanorod growth direction, due to the intrinsic polar crystal structure, ZnO4 tetrahedral. In addition, such an internal electric field may retard or inhibit the charge recombination [36]. However, single crystal ZnO nanorods inherit the same surface challenges of ZnO nanoparticles; the hydroxyl groups, oxygen vacancies and organic residuals commonly lead to unacceptable device instability when used as electron transporting layer in perovskite solar cells [37–42]. Strategies to address the above-mentioned problems include removal of OH^- groups and residual chemicals on ZnO surface by heating at high temperatures [41], deposition of an intermediate polymer layer to block the direct interaction between perovskite and ZnO [42,43], and doping of aluminum to improve the surface property [44]. They potentially restrain the recombination at the ZnO/perovskite interface, however, there is no report on raising the durability of $CH_3NH_3PbI_3$ on ZnO NRs in the ambient environment.

To resolve the decomposition and raise the durability of perovskite absorbers on the ZnO nanorods surface, SnO_2 film has been chosen as a passivation layer, because of its wide band gap, matching with that of perovskite and ZnO, low chemical reactivity, high stability under UV illumination and excellent durability in the ambient environment [45–48]. SnO_2 has been studied as both ETLs and antireflection films in PSCs with enhanced power conversion efficiency [49–54]. SnO_2 has also showed the potential to fabricate planar devices with long term air stability and suppressed hysteresis [55–57]. Thus, the insufficiency of each ETL material (ZnO NRs or SnO_2) investigated in PSCs further develop ETL by combing two semiconductors into one with strong encouragement, so that ZnO NRs and SnO_2 can compensate each other.

In this work, core-shell ZnO@SnO_2 nanorods have been fabricated by depositing SnO_2 passivation layer on the ZnO nanorods surface, and investigated the surface chemistry and the thermal stability of $CH_3NH_3PbI_3$ films grown on ZnO NRs and ZnO@SnO_2 NRs substrates. The SnO_2 passivation layer has been found to effectively suppress the degradation of $CH_3NH_3PbI_3$ perovskite, and perovskite solar cells with SnO_2 passivation coating on ZnO nanorods as electron transporting layer are far more efficient in photo-to-electricity conversion and also hysteresis-free. The power conversion efficiency of perovskite solar cells was increased from 6.92% to 12.17% by applying SnO_2 passivation layer on ZnO NRs surface.

2. Experimental

2.1. Preparation of ZnO dense layer

First, we sputtered a dense layer of intrinsic ZnO nanoparticle on a glass substrate coated with cleaned fluorine doped tin oxide (FTO). 1.8 g Zn $(CH_3COO)_2$ was dissolved in 50 mL deionized water with stirring for 60 min to form an emulsion solution, To form a clear precursor solution, 0.881 g diethanolamine was added with stirring for 60 min. Finally, sintered at 500 °C for 30 min to obtain a dense layer after spin coating at 3500 rpm for 25 s.

2.2. ZnO nanorods growth

ZnO nanorods were electrochemically grown in an aqueous solution inside a three-electrode cell. The growth solution was prepared by incorporating a 0.01 M aqueous solution $Zn(NO_3)\cdot 6H_2O$ and 0.01 M aqueous solution of methenamine and quickly heating up the solution to 70 °C on a hot plate. A platinum wire immersed in the solution was used as a counter electrode. An Ag/AgCl electrode in saturated KCl (3 M) was used as the reference electrode. A negative DC potential of −1.0 V relative to the reference electrode was applied to a soda lime glass coated with fluorine doped tin oxide (FTO), which were used as substrates. After a 1 h growth time, the samples were immediately rinsed with deionized water. Sintered at 500 °C for 30min to obtain the final ZnO NRs.

2.3. Preparation of core-shell ZnO nanorods (ZnO@SnO_2 NRs)

A precursor solution was prepared by dissolving 0.2 mol/L $SnCl_2$ in ethanol with stirring for 30 min, sintered at 500 °C for 30 min after spin coating at 4000 rpm for 60 s on the ZnO NRs substrate.

2.4. Perovskite solar cell fabrication

PbI_2 was dissolved in DMF at a concentration of 462 mg ml^{-1}(1 M) with stirring at 70 °C, to obtain a homogeneous CH_3NH_3I solution around the FTO substrate. The solution was maintained at 70 °C during the whole procedure. The ZnO NRs films with modified-SnO_2 layer or not were then infiltrated with PbI_2 by spin coating at 6000 rpm for 10 s and dried. The films were then dipped in a solution of CH_3NH_3I in 2-propanol (10 mg ml^{-1}) for 10 min, respectively, rinsed with 2-propanol and dried at 70 °C for 30 min. The HTM was then deposited by spin coating at 4000 rpm for 30 s. The spin-coating formulation was prepared by dissolving 72.3 mg (2,2′,7,7′-tetrakis(*N*,*N*-di-*p*-methoxyphenyl-amine)-9,9-spirobifluorene)(spiro-MeOTAD), 28.8 μl 4-*tert*-butylpyridine, 17.5 μl of a stock solution of 520 mg ml^{-1} lithium bis(trifluoromethylsulphonyl)imide in acetonitrile in 1 ml chlorobenzene. For fabrication, the perovskite film and HTM were prepared in a glove box. Finally, 150 nm Ag was thermally evaporated onto the HTM layer under vacuum to act as the cathode. The cell area is 0.07065 cm^2.

2.5. Characterization

The transmission electron microscopy (TEM) measurements were carried out with JEOL JEM-2100F under the voltage of 200 kV, Scanning Electron Microscopy (SEM) measurements conducted were Hitachi-S-4800. The X-ray diffraction (XRD) measurements were performed on a D8 Advance (Germany) diffractometer with Cu Kα radiation (40 kV and 40 mA) and the scanning rate of 4° min^{-1} for wide angle test increment over the Bragg angle range of 10–70°. Ultraviolet–visible spectroscopy (UV–Vis) transmittance/absorbance and time-resolved photoluminescence spectroscopy (TRPL) spectra were recorded with a Shimadzu UV-2550 (300–600 nm: xenon lamp, 300 W; 600–900 nm: tungsten–halogen lamp, 150 W) and Fls-800 spectrometers, respectively. Raman spectroscopy was obtained on a DXR Raman microscope with an excitation length of 532 nm. The photo-current–voltage (J–V) characteristics of the solar cells were measured using a Keithley 2400 source under illumination of a simulated sunlight (AM1.5, 100 mW cm^{-2}) provided by a solar simulator (Newport 69907) with an AM1.5 filter. The light intensity was adjusted with an NREL-calibrated Si solar cell with a KG-2 filter for approximating 1 sunlight intensity. While measuring current and voltage, the cell was covered with a black mask with an aperture (aperture area is close

to the active device area). The incident photon-to-current efficiency (IPCE) was measured in DC mode with a 1/4 m double monochromatography (Crowntech DK242), a multimeter (Keithley 2000), and two light sources depending on the wavelength range required (300–600 nm: xenon lamp, 300 W; 600–900 nm: tungsten–halogen lamp, 150 W). The monochromatic light intensity for IPCE efficiency was calibrated with a reference silicon photodiode. All the measurements of the solar cells were performed under an ambient atmosphere at room temperature without encapsulation.

3. Results and discussion

The schematic illustration of perovskite solar cell architecture based on ZnO@SnO_2 nanorods (FTO/ZnO@SnO_2 NRs/$CH_3NH_3PbI_3$/Spiro-OMETAD/Ag) and energy level diagrams of related materials are displayed in Fig. 1a and b. The core-shell arrays in Fig. 1a were made up of ZnO nanorod as the core and SnO_2 thin film as the shell. The perovskite solar cell with FTO/ZnO@SnO_2 NRs/$CH_3NH_3PbI_3$/Spiro-OMETAD/Ag stacking structure is shown in the color-enhanced cross-sectional scanning electron microscopy (SEM) image in Fig. 1c. ZnO NRs were fabricated by electrochemical deposition, and the SnO_2 film synthesized by spin-coating. The $CH_3NH_3PbI_3$ perovskite was formed by two-step sequential deposition method and then spiro-MeOTAD film as the hole-transporting layer (HTL) was spin-coated on the perovskite film, finally Ag film was evaporated on spiro-OMeTAD film.

Fig. 2a shows a typical *J–V* curve of ZnO NRs based perovskite solar cells, exhibiting large hysteresis with respect to scan directions and the performance parameters are summarized in Table 1. The open circuit voltage in the reverse scan is 0.03 V greater than the open circuit voltage (V_{oc}) by the forward scan. In addition, both short circuit current density (J_{sc}) and filled factor (FF) in the reverse scan were found greater than that in the forward scan, reduced from 21.15 to 19.43 mA/cm^2 and from 57.3 to 43.4%, respectively. The great hysteresis in the *J–V* curve is also reflected by the big difference in PCE: 10.23% in forward scan and 6.92% in reverse scan. Fig. 2b shows the typical *J–V* curve of ZnO@SnO_2 NRs-based perovskite solar cells, without obvious hysteresis, and the performance parameters are also summarized in Table 1. The PCE has been enhanced from 10.23% to 12.17% by depositing SnO_2 layers on ZnO NRs. Fig. 2c compares the dark *J–V* characteristics of PSCs based on ZnO NRs and ZnO@SnO_2 NRs. The charge recombination in the ZnO@SnO_2 NRs solar cell could be suppressed compared with the ZnO NRs based devices, resulting in a considerably lower back current density in the ZnO@SnO_2 NRs solar cells in Fig. 2c.

Although SnO_2 has a more negative CB energy level than that of ZnO, and SnO_2 layer can not completely prevent the occurrence of charge recombination, SnO_2 layer causing a smaller current loss might be attributed to its much higher electron mobility, which has been proved and widely used in perovskite solar cells as an electron transport material [48–55]. We note that the existence of SnO_2 showing faster transferring ability of photoinduced electrons (Fig. S5) is beneficial for providing balanced carrier transport within the perovskite absorber, which is responsible for the low hysteresis observed. Unbalanced carrier transport within the perovskite absorber has been considered an important mechanism causing J-V hysteresis [74,75].

A diode-like behavior can be seen for both solar cells. The reverse bias saturation current density (J_o) of the ZnO@SnO_2 nanorods-based solar cell is significantly lower than that of the ZnO NRs solar cell, thereby leading to a larger open circuit voltage (V_{oc}) of the ZnO@SnO_2 NRs solar cell, agreeing with the *J-V* results (shown in Table 1), which is estimated according to the well-known relationship [58].

$$V_{oc} = \left(\frac{nkT}{q}\right)\ln\left(\frac{J_{ph}}{J_0} + 1\right)$$

Where J_{ph} is the photocurrent density, which is generally equal to the short-circuit current density (J_{sc}), J_o is the (reverse bias) saturation current density, q is the charge of an electron, n is the

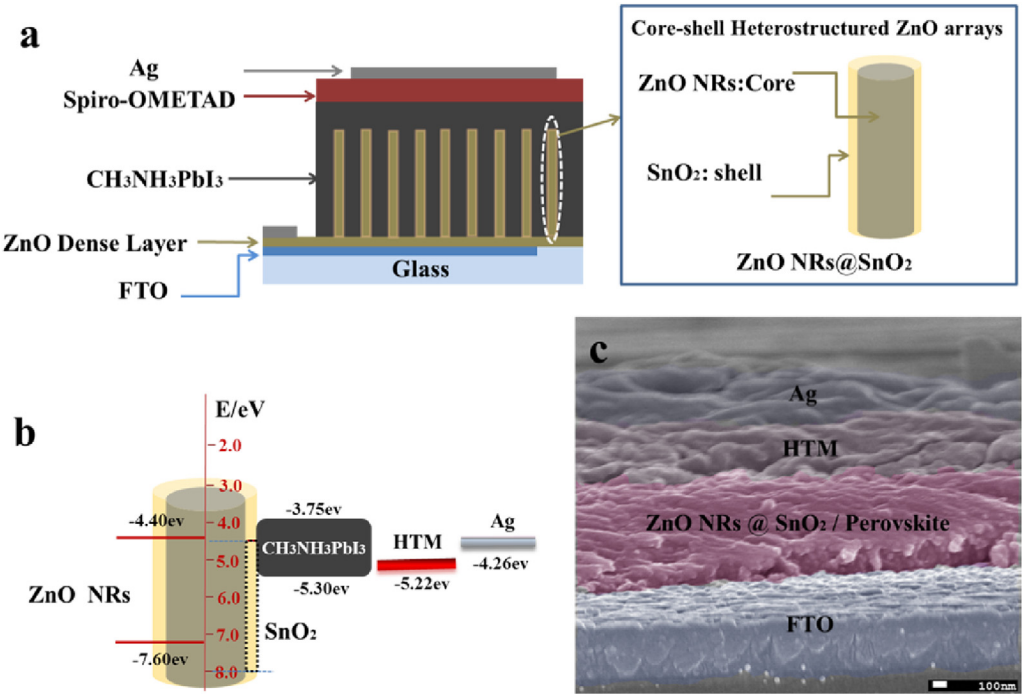

Fig. 1. (a), Schematics of device structure based on core-shell heterostructured ZnO arrays (the inset shows the schematic representation of SnO_2 as shell structure: ZnO NRs@SnO_2). (b), Energetic diagram of the devices. (c), SEM cross-sectional image of representative solar cell.

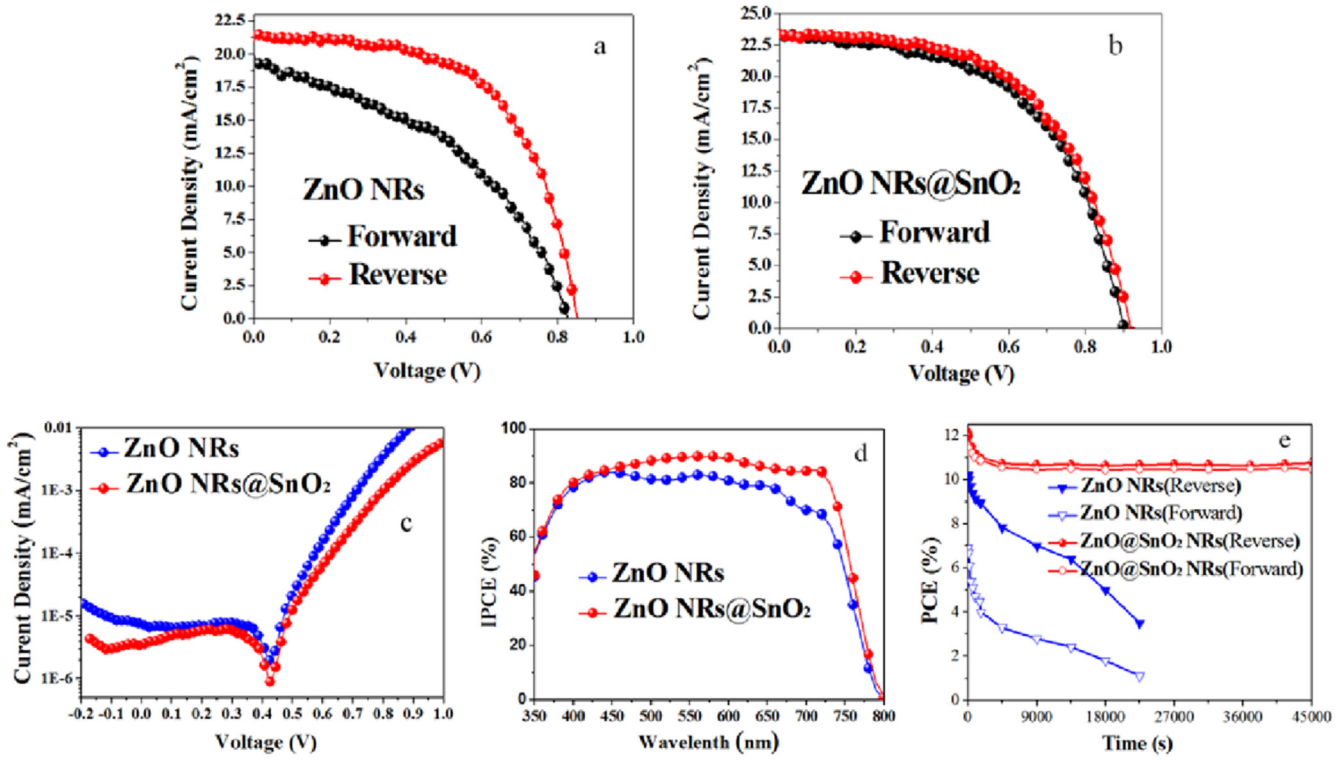

Fig. 2. J–V curves of perovskite hybrid solar cells for (a) bare ZnO NRs substrate and (b) ZnO@SnO_2 NRs substrate which measured by forward and reverse scans; (c) Dark current measurements; (d) IPCE spectra of perovskite solar cell devices and (e) Durability of perovskite solar cell devices. All J-V curves were measured under 100 mW/cm^2 air mass 1.5 global (AM 1.5G) illumination.

ideality factor, k is the Boltzmann constant, and T is the absolute temperature. This means that the V_{oc} may increase with the improving of the photocurrent density (J_{ph}) in consistent with the photovoltaic performance in Table 1.

The incident-photon-to-current efficiency (IPCE) for both ZnO NRs and ZnO@SnO_2 NRs are shown in Fig. 2d. The integrated photocurrent from the IPCE is in good agreement with the measured J_{sc} value for ZnO NRs and ZnO@SnO_2 NRs. The long term stability as a function of time was performed, and the results are shown in Fig. 2e. Power output of the ZnO@SnO_2 NRs based cell remained stable within 45000 s (12.5 h), with a stable PCE of 12.17%. In contrast, the ZnO NRs solar cells showed a rapid and drastic decrease in PCE. The significant difference in long-term stability in ZnO@SnO_2 NRs suggests that the SnO_2 passivation layer introduced a mechanism to stabilize perovskite solar cell devices.

By comparing top view SEM images and the cross-sectional SEM EDS mapping showed in Fig. 3 and Fig. S1-S2, a conformal SnO_2 shell is homogenously deposited on the surface of ZnO NRs to form a core–shell structure, which is in consistent with the transmission electron microscope (TEM) images in Fig. 4. The composition and the atomic value of core-shell ZnO@SnO_2 NRs, especially of Sn were characterized by means of X-ray Photoelectron Spectroscopy (XPS) and the spectra were shown in Fig. 3c and S3. The full XPS spectrum in the range of 0–1200eV given in Fig. S3a shows the presence of O, Sn, Zn and C. The binding energies of 486.8 and 495.2 eV corresponding to Sn $3d_{5/2}$ and Sn $3d_{3/2}$ were highlighted in Fig. 3c, respectively. The formation of SnO_2 passivation layer was readily confirmed with the presence of Sn^{4+} peaks [59], which corroborates well with the XRD patterns presented in Fig. 3d. The binding energies of 1022.00 and 1045.15 correspond to Zn $2P_{3/2}$ and Zn $2P_{1/2}$, respectively as shown in Fig. S3c. The main binding energy of 530.48 eV is attributed to O 1s, which is the O^{2-} state in ZnO and SnO_2 (Fig. S3d). The binding energy of O 1s can be assigned to the chemisorbed oxygen atoms or hydroxyl groups [60], which will be discussed in detail later in this article. XRD patterns of FTO, FTO/ZnO NRs and FTO/ZnO@SnO_2 NRs were showed in Fig. 3d. The diffraction peaks at 34.5°, 36.3°, 47.6°, 62.9° can be well assigned to Wurtzite ZnO.

Fig. 4 show the transmission electron microscopy (TEM) images of core-shell ZnO@SnO_2 NRs, and SnO_2 shell was easily distinguished from ZnO nanorods. High-resolution transmission electron microscopy (HR-TEM) images in Fig. 4b and c clearly show the interface between ZnO NRs core and SnO_2 shell, and the lattice fringes of SnO_2 have a small angle deviation in comparison with lattice fringes of ZnO NRs in Fig. 4b. Highly crystallized SnO_2 shell with a thickness of about 3 nm conformally grown on the surface of ZnO NRs arrays. The energy-dispersive spectroscopy (EDS) results of the sample ZnO@SnO_2 NRs in Fig. 4d demonstrated the existence of O, Zn, Sn elements with a ratio of O/Zn/Sn is 54.32:44.25:1.43.

With the much improvement of the efficiency of perovskite solar cell, an increasing attention has been paid to the stability performance, especially the chemical stability of perovskite materials. The performance stability of perovskite solar cells is the key

Table 1
Comparison of photovoltaic parameters of perovskite solar cells with ZnO nanorod arrays and ZnO@SnO_2 core-shell nanorod arrays as electron transport layers with forward and reverse scans.

ETL	Scan direction	*Voc* (V)	*Jsc* (mA/cm^2)	*FF* (%)	PCE (%)
ZnO NRs @ SnO2	Forward	0.899	23.28	55.1	11.55
	Reverse	0.909	23.31	57.4	12.17
ZnO NRs	Forward	0.819	19.43	43.4	6.92
	Reverse	0.849	21.15	57.3	10.23

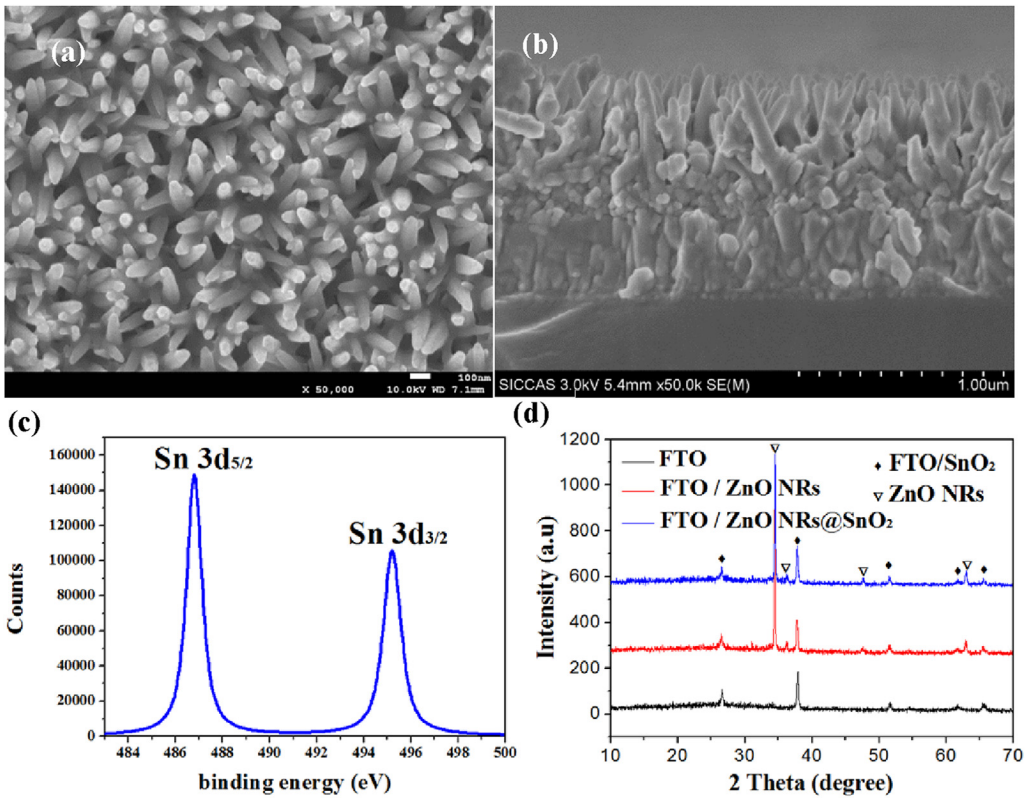

Fig. 3. Top view SEM images (a) of ZnO@SnO_2 NRs, and cross-sectional SEM (b) of ZnO@SnO_2 NRs, XPS spectra (c) of Sn 3d of ZnO@SnO_2 NRs on the glass substrate, XRD pattern (d) of FTO, FTO/ZnO NRs and FTO/ZnO@SnO_2 NRs.

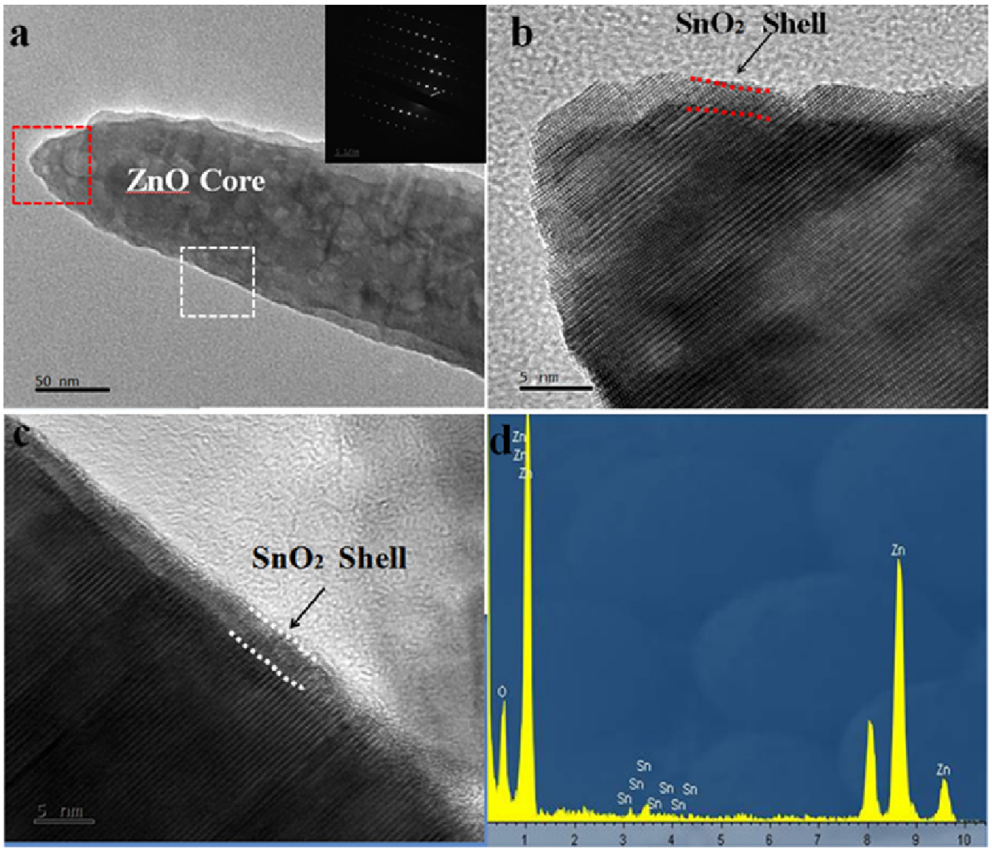

Fig. 4. TEM image (a) of a single core-shell ZnO@SnO_2 nanorods and corresponding FFT pattern, (b) HR-TEM images taken from the area masked by a red square in (a); (c) HR-TEM images taken from the area masked by a white square in (a), (d) simultaneous energy-dispersive spectroscopy (EDS) of the ZnO@SnO_2 NRs.

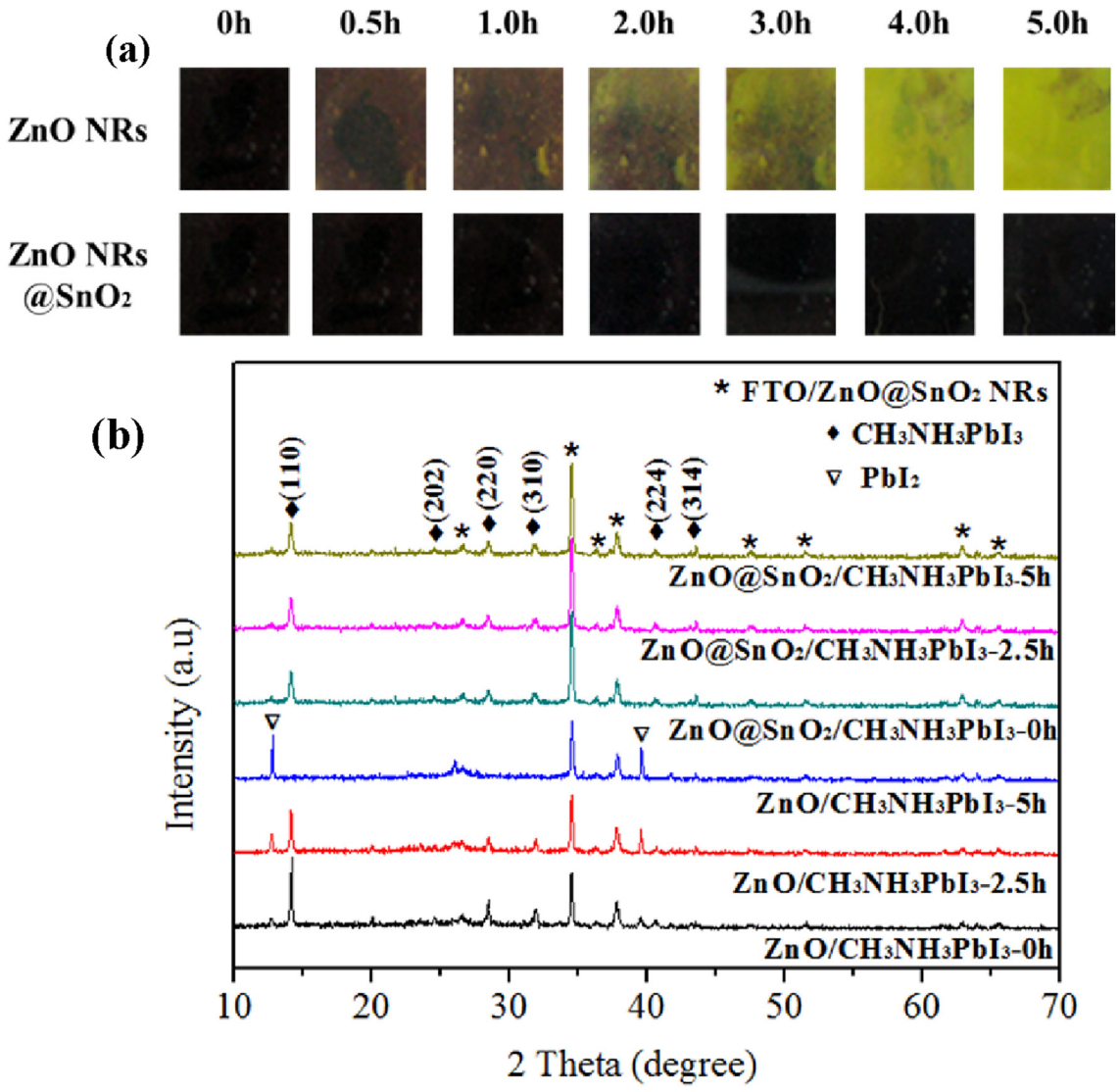

Fig. 5. The photographs (a) and XRD patterns (b) of perovskite layers deposited on bare ZnO NRs and ZnO@SnO_2 NRs with different thermal annealing time from 0 to 5 h in air at 100 °C.

factor limiting the potential success in commercialization of perovskite solar cells. The stability of perovskite solar cells is closely related to the surrounding environment, such as oxygen and moisture, sun light, and temperature etc. The present investigation revealed the thermal instability on $CH_3NH_3PbI_3$ thin films deposited on ZnO NRs substrates as shown in Fig. 5a, similar to what reported in literature [61]. The fresh $CH_3NH_3PbI_3$ films deposited on ZnO NRs were dark brown, but yellow spots began to appear, extending yellow spots gradually when subjected to heat-treatment at 100 °C, till $CH_3NH_3PbI_3$ films completely decomposed to PbI_2, CH_3NH_2 (gas) and H_2O (gas) as revealed by the XRD patterns presented in Fig. 5b.

XRD patterns in Fig. 5b showed the evolution of crystalline phases when $CH_3NH_3PbI_3$ perovskite film grown on ZnO NRs annealed at 100 °C. After 5 h, diffraction peaks of perovskite disappeared, and new PbI_2 diffraction peaks were observed. Peaks located at 12.6° and 39.5° are assigned to (001) and (003) lattice planes of the PbI_2 (JPCDS card No. 73–1750) [4], while the peaks at 14.2°, 24.6°, 28.5°, 31.9°, 40.6°, and 43.2° are corresponding to the reflections from [110], [202], [220], [310], [224], and [314] planes of the $CH_3NH_3PbI_3$ perovskite [62]. In a sharp contrast, the color of $CH_3NH_3PbI_3$ films deposited on ZnO@SnO_2 NRs remained almost unchanged dark brown. The results suggested that $CH_3NH_3PbI_3$ is sensitive to the surface of ZnO NRs, and the SnO_2 layer with a passivating function when subjected to thermal annealing at 100 °C.

Transmission spectra and absorption spectra of ZnO NRs and ZnO@SnO_2 NRs without $CH_3NH_3PbI_3$ perovskite films were presented in Fig. 6 and Fig. S4. No appreciable difference in transmission and absorbance properties was observed between ZnO@SnO_2 NRs and ZnO NRs as shown in Fig. 6a. This suggests that SnO_2 shell did not decrease the light transmission, the results are easily to understand considering the fact that SnO_2 possesses a larger bandgap than that of ZnO and the SnO_2 is only a few nanometer in thickness.

The steady photoluminescence spectra of $CH_3NH_3PbI_3$ films were acquired after thermal annealing at 100 °C in air with various duration time, and the results are summarized in Fig. 6c. Initially, $CH_3NH_3PbI_3$ films showed the characteristic absorption character with an absorption edge at 780 nm. Light absorbance of $CH_3NH_3PbI_3$ films on ZnO nanorods decreased gradually with increased annealing time. The value of $CH_3NH_3PbI_3$/ZnO film after

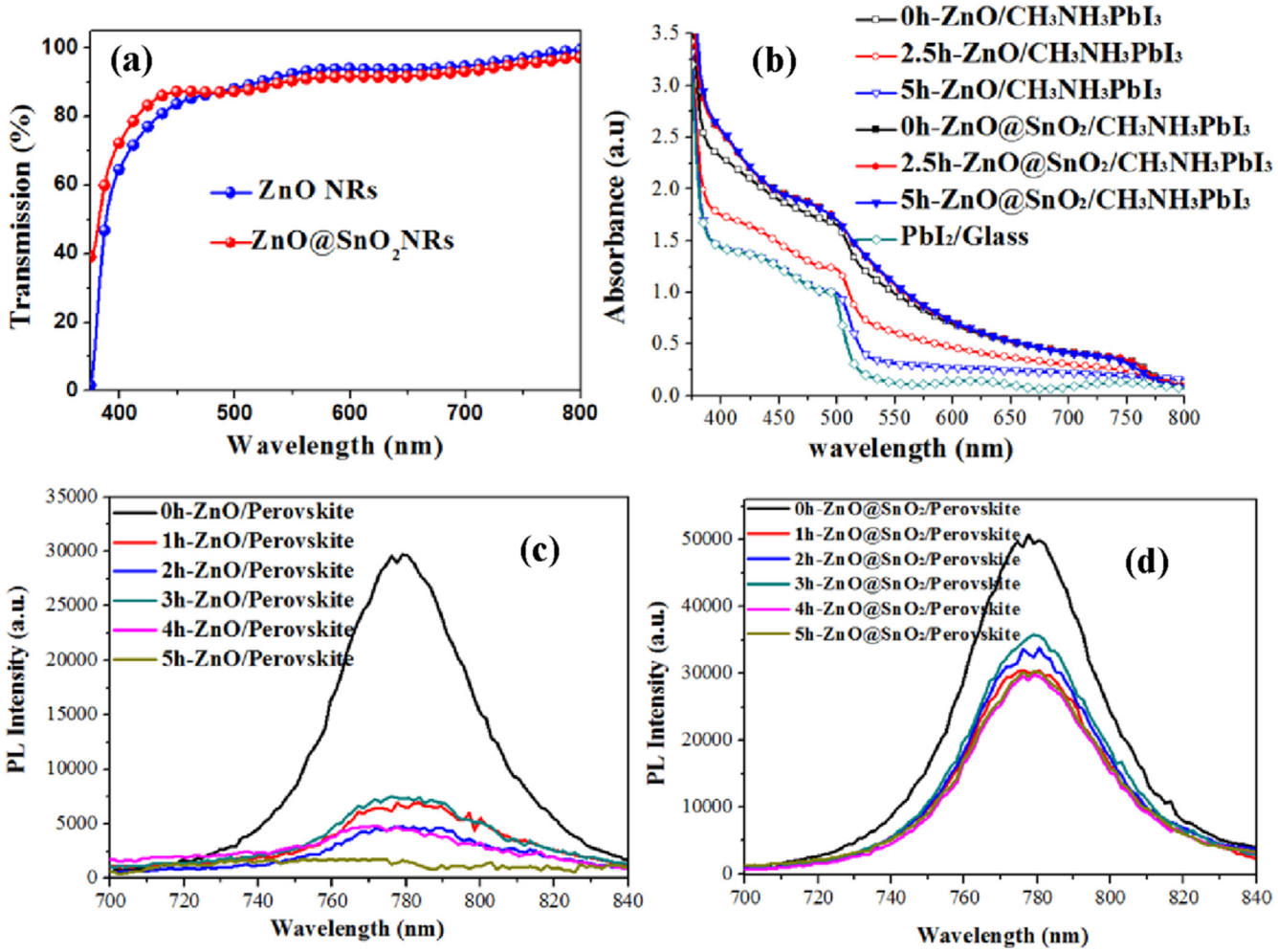

Fig. 6. (a) Transmission spectra of ZnO NRs film and ZnO@SnO_2 NRs film without perovskite films. (b) Absorbance spectra of ZnO NRs/$CH_3NH_3PbI_3$ film and ZnO@SnO_2 NRs/$CH_3NH_3PbI_3$ film with thermal annealing at 100 °C in different time. PL spectra of $CH_3NH_3PbI_3$ films deposited on (c) ZnO NRs substrate and (d) ZnO@SnO_2 NRs substrate annealed at 100 °C for different duration of time.

2.5 h thermal annealing decreased by more than half, and the absorption character of $CH_3NH_3PbI_3$/ZnO at 780 nm disappeared after 5 h annealing. The perovskite film on ZnO NRs in the end decomposed into a yellow colored by product consistent with the absorbance wavelength (530 nm) of PbI_2 in Fig. 6b, and this is in agreement with Yan group [59]. In contrast, there is no apparent decrease in the absorbance for $CH_3NH_3PbI_3$ on ZnO@SnO_2 NRs substrates at 780 nm during 5 h thermal annealing, which matched well with the photo results and XRD pattern in Fig. 5. This suggests the existence of SnO_2 shell plays an important role to prevent $CH_3NH_3PbI_3$ film decay to PbI_2.

In order to study exciton diffusion, time-resolved photoluminescence (TRPL) decay is investigated in Fig. S5. The time-resolved PL decay curves monitored at the wavelength of 507 nm, extracted from the perovskite films on ZnO NRs and ZnO@SnO_2 NRs. The carrier lifetime of $CH_3NH_3PbI_3$ layer on ZnO@SnO_2 NRs is reduced and displayed a TRPL decay faster than that on the ZnO NRs. This advantage can be regarded as a factor that results in high J_{sc} of ZnO@SnO_2 NRs solar cell in according with photovoltaic performance as presented in Fig. 2 and Table 1.

Fig. 6c and d show the steady state photoluminescence (PL) spectra of the $CH_3NH_3PbI_3$/ZnO NRs and $CH_3NH_3PbI_3$/ZnO@SnO_2 NRs. PL spectra of $CH_3NH_3PbI_3$ at 525 nm were collected with increasing annealing time. The quenching of $CH_3NH_3PbI_3$ photoluminescence on ZnO NRs increases as a function of time as shown in Fig. 6c, and the quenching of the $CH_3NH_3PbI_3$ perovskite PL on ZnO NRs is totally completed after 5 h thermal annealing. In contrast, as shown in Fig. 6d, maximal quenching of $CH_3NH_3PbI_3$ PL on ZnO@SnO_2 NRs is rapidly reached 58.2% and no further increases were seen within our experimental time frame. The electron transfer from excited states in $CH_3NH_3PbI_3$ perovskite to ZnO NRs is very weak with the annealing time increased from 0 h to 5 h. Whereas the SnO_2 shell keeps the stability of the electron transfer on the $CH_3NH_3PbI_3$/SnO_2 interface from 2 h to 5 h annealing. This suggests the hydroxyl group or oxygen vacancies on the surface of SnO_2 could react with the $CH_3NH_3PbI_3$ and affect the decomposition of $CH_3NH_3PbI_3$ film, as reported in literatures [41,63].

To obtain an insight of the decomposition of $CH_3NH_3PbI_3$ on respective ZnO NRs and ZnO@SnO_2 NRs layers, the chemical structure of ZnO NRs and ZnO@SnO_2 NRs surfaces was investigated by means of X-ray photoelectron spectroscopy (XPS) with the results presented in Fig. 7. The Gaussian-resolved result for O 1s spectra in Fig. 7a–b shows that the oxygen peak can be consistently fitted by three nearly Gaussian components, centered at 530.30 eV (O_I), 531.00 eV (O_{II}), and 531.90 eV (O_{III}). These peaks can be ascribed to O^{2-} ions (O_I) in wurtzite structure of ZnO, O^{2-} (O_{II}) in the oxygen vacancy regions ($V_O^{\bullet\bullet}$), and the chemisorbed oxygen species (O_{III}) such as hydroxyl group (OH^-). With passivating SnO_2 shell on the

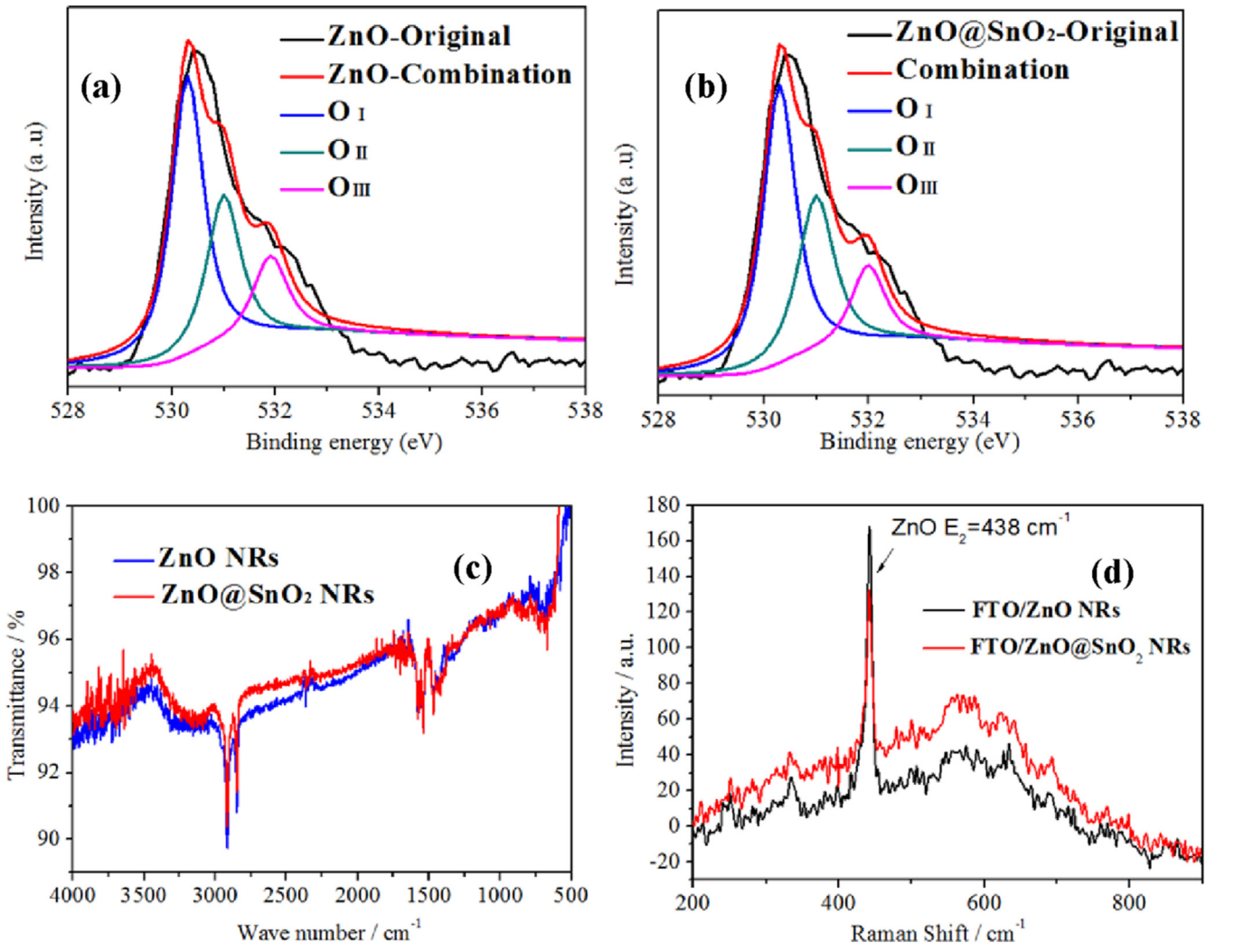

Fig. 7. High-resolution of O 1s XPS spectra of (a) bare ZnO NRs and (b) ZnO@SnO_2 NRs; FT-IR spectra (c) of ZnO NRs and ZnO@SnO_2 NRs; Raman spectra (d) for ZnO NRs and ZnO@SnO_2 NRs.

ZnO NRs, the ratio of O in hydroxyl (O_{III}) decreased from 17.0% to 15.6%; while the oxygen vacancy (O_{II}) increased from 29.8% to 32.5%. Generally, hydroxyl (OH^-) groups on the ZnO NRs surface have been considered to initiate the decomposition of $CH_3NH_3PbI_3$ perovskite [41,42,61]. However the ratio of the hydroxyl (OH^-) groups is almost the same on both surfaces of ZnO NRs and ZnO@SnO_2 NRs, so the hydroxyl (OH^-) groups might not be the only cause of perovskite $CH_3NH_3PbI_3$ decomposition or the hydroxyl groups at different surfaces may possess different chemical reactivity.

The underlying reasons for the improved stability of the $CH_3NH_3PbI_3/SnO_2$ interface may be attributed to: (1) photoelectrochemical, electromechanical, and/or electromigration processes [64–66], (2) accumulated negative charge and ion migration at the SnO_2/perovskite interface inducing a high electric field and/or dipole formation [67–69], (3) lower hygroscopicity, oxygen vacancies and UV light induced degradation of perovskite [52] and (4) wide band gap of SnO_2 and good band edge matching with $CH_3NH_3PbI_3$ perovskite that reduce energy loss for photogenerated electrons with good blocking effects for holes [53].

The above mechanisms, however, could not explain the experimental results from this work, the amount of hydroxyl groups was found to be the same on the surface of ZnO NRs and ZnO@SnO_2 NRs. Although the exact mechanism requires further investigation, the much enhanced thermal stability of $SnO_2/CH_3NH_3PbI_3$ interface might be ascribed to the result of hydroxyl groups trapped at oxygen vacancies on the surface of SnO_2, and the bond strength of Sn–OH is greater than that of Zn–OH. SnO_2 layer is using for providing inactive surface hydroxyl groups and formatting an isolating layer rather than formatting potential barrier between ZnO and perovskite. In addition, the energy level of SnO_2 CB is not that much different with ZnO CB, So SnO_2 was used for modifying layer and passivation layer in our group. To further confirm the hypothesis that the hydroxide and the oxygen vacancy on the ZnO@SnO_2 NRs surface, Fourier Translation Infrared Spectroscopy (FT-IR) and Raman spectra were collected on both samples and the results are presented in Fig. 7. As shown in Fig. 7c, the IR shift around 3214 and 2912 cm^{-1} from the stretching modes of surface hydroxyl groups suggest that the mount of hydroxyl ligands is nearly the same in agreement with the XPS results in Fig. 7a and b [70–72]. Fig. 7d exhibits the Raman spectra of the ZnO NRs and ZnO@SnO_2 NRs, and the 438 cm^{-1} mode corresponds to the E_2 mode for Wurtzite ZnO crystal with very sharp features. No obvious Raman peak of SnO_2 appeared in the spectra of the FTO (F:SnO_2)/ZnO@SnO_2 NRs, indicating no secondary phase in FTO/ZnO@SnO_2 NRs samples, which is consistent with the XRD patterns of FTO/ZnO@SnO_2 NRs in Fig. 3d. With the SnO_2 passivation, peak around

400–700 cm^{-1} was conjectured to be associated with intrinsic lattice defects and hydroxyl metal complex in agreement with Cs symmetry [73], indicating the OH^- exists in the $V_O^{\bullet\bullet}$ state on the SnO_2 shell surface. Strong interaction of hydroxyl groups with oxygen vacancies may substantially reduce the reactivity of hydroxyl groups on the surface of SnO_2, and consequently lead to much enhanced thermal stability in $SnO_2/CH_3NH_3PbI_3$ interface and suppressed decomposition of $CH_3NH_3PbI_3$ commonly observed on ZnO NRs surface.

4. Conclusions

A core-shell ZnO@SnO_2 nanorods film has been successfully utilized in the $CH_3NH_3PbI_3$ perovskite solar cell as an electron transporting material. By depositing the highly crystallized SnO_2 layer on ZnO nanorods, the decomposition of $CH_3NH_3PbI_3$ perovskite was prevented, and the perovskite solar cell exhibited an increased PCE of 12.17% with negligible hysteresis. The steady photoluminescence, UV–Vis absorbance and X-ray diffraction patterns indicated that the formation of $CH_3NH_3PbI_3$ is very sensitive to the surface chemistry and morphology of ZnO NRs, and SnO_2 passivation layer suppresses the decomposition of $CH_3NH_3PbI_3$ to PbI_2. Although the amount of hydroxyl groups is the same on both ZnO NRs and ZnO@SnO_2 NRs surfaces, OH^- groups strongly interact with oxygen vacancies on SnO_2 surface and thus compromised their chemical reactivity. Consequently the introduction of SnO_2 passivation layer resulted in much enhanced thermal stability of $CH_3NH_3PbI_3$ films.

Acknowledgments

The University of Washington, in particular Prof. Jiangyu Li and Dr. Zonglong Zhu are thanked for discussion with Dr. Zhao. The authors thank the financial support from National Key Research and Development Program of China (2016YFA0201001), National Natural Science Foundation of China (11627801, 51102172), Science and Technology Plan of Shenzhen City (JCYJ20160331191436180), National Program on Key Basic Research Project (973 Program, 2014CB260405), Natural Science Foundation for Outstanding Young Researcher in Hebei Province (E2016210093), The Key Program of Educational Commission of Hebei Province of China (ZD2016022), The Youth Top-notch Talents Supporting Plan of Hebei Province, China Scholarship Council (CSC No. 201508130032), Hebei Provincial Key Laboratory of Traffic Engineering materials, Hebei Key Discipline Construction Project.

Appendix A. Supplementary data

Supplementary data related to this article can be found at http://dx.doi.org/10.1016/j.jpowsour.2016.11.046.

References

[1] A. Kojima, K. Teshima, Y. Shirai, T. Miyasaka, J. Am. Chem. Soc. 131 (2009) 6050–6051.
[2] H.-S. Kim, C.-R. Lee, J.-H. Im, K.-B. Lee, T. Moehl, A. Marchioro, S.-J. Moon, R. Humphry-Baker, J.-H. Yum, J.E. Moser, M. Gratzel, N.-G. Park, Sci. Rep. 2 (2012) 591.
[3] M.M. Lee, J. Teuscher, T. Miyasaka, T.N. Murakami, H.J. Snaith, Science 338 (2012) 643–647.
[4] J. Burschka, N. Pellet, S.-J. Moon, R. Humphry-Baker, P. Gao, M.K. Nazeeruddin, M. Gratzel, Nature 499 (2013) 316–319.
[5] M.B.J. Mingzhen Liu, Henry J. Snaith, Nature 501 (2013) 395–398.
[6] H. Zhou, Q. Chen, G. Li, S. Luo, T.-b. Song, H.-S. Duan, Z. Hong, J. You, Y. Liu, Y. Yang, Science 345 (2014) 542–546.
[7] N.J. Jeon, J.H. Noh, W.S. Yang, Y.C. Kim, S. Ryu, J. Seo, S.I. Seok, Nature 517 (2015) 476–480.
[8] W.S. Yang, J.H. Noh, N.J. Jeon, Y.C. Kim, S. Ryu, J. Seo, S.I. Seok, Science 348 (2015) 1234–1237.
[9] W. Nie, H. Tsai, R. Asadpour, J.-C. Blancon, A.J. Neukirch, G. Gupta, J.J. Crochet, M. Chhowalla, S. Tretiak, M.A. Alam, H.-L. Wang, A.D. Mohite, Science 347 (2015) 522–525.
[10] C. Yi, X. Li, J. Luo, S.M. Zakeeruddin, M. Grätzel, Adv. Mater. 28 (2016) 2964–2970.
[11] J.S. Junyan Xiao, Dongmei Li, Qingbo Meng, Sci. China Chem. 58 (2015) 221–238.
[12] Q. Wang, H. Chen, G. Liu, L. Wang, Sci. Bull. 60 (2015) 405–418.
[13] L. Ye, B. Fan, S. Zhang, S. Li, B. Yang, Y. Qin, H. Zhang, J. Hou, Sci. China Mater. 58 (2015) 953–960.
[14] Q. Zhang, C.S. Dandeneau, X. Zhou, G. Cao, Adv. Mater. 21 (2009) 4087–4108.
[15] D. Zhong, B. Cai, X. Wang, Z. Yang, Y. Xing, S. Miao, W.-H. Zhang, C. Li, Nano Energy 11 (2015) 409–418.
[16] J.T.-W. Wang, J.M. Ball, E.M. Barea, A. Abate, J.A. Alexander-Webber, J. Huang, M. Saliba, I. Mora-Sero, J. Bisquert, H.J. Snaith, R.J. Nicholas, Nano Lett. 14 (2013) 724–730.
[17] J. Zhao, P. Wang, L. Wei, Z. Liu, X. Fang, X. Liu, D. Ren, Y. Mai, Dalton Trans. 44 (2015) 16914–16922.
[18] B. Li, J. Tian, L. Guo, C. Fei, T. Shen, X. Qu, G. Cao, ACS Appl. Mater. Interfaces 8 (2016) 4684–4690.
[19] Z. Zhao, X. Chen, H. Wu, X. Wu, G. Cao, Adv. Funct. Mater. 26 (2016) 3048–3058.
[20] Ü. Özgür, Y.I. Alivov, C. Liu, A. Teke, M.A. Reshchikov, S. Doğan, V. Avrutin, S.-J. Cho, H. Morkoç, J. Appl. Phys. 98 (2005) 041301.
[21] H. Tang, K. Prasad, R. Sanjinès, P.E. Schmid, F. Lévy, J. Appl. Phys. 75 (1994) 2042–2047.
[22] H.S. Bae, M.H. Yoon, J.H. Kim, S. Im, Appl. Phys. Lett. 83 (2003) 5313–5315.
[23] J. Zhang, T. Pauporté, J. Phys. Chem. C 119 (2015) 14919–14928.
[24] F. Guo, H. Azimi, Y. Hou, T. Przybilla, M. Hu, C. Bronnbauer, S. Langner, E. Spiecker, K. Forberich, C.J. Brabec, Nanoscale 7 (2015) 1642–1649.
[25] Z.-L. Tseng, C.-H. Chiang, C.-G. Wu, Sci. Rep. 5 (2015) 13211.
[26] J. Kim, G. Kim, T.K. Kim, S. Kwon, H. Back, J. Lee, S.H. Lee, H. Kang, K. Lee, J. Mater. Chem. A 2 (2014) 17291–17296.
[27] D. Liu, M.K. Gangishetty, T.L. Kelly, J. Mater. Chem. A 2 (2014) 19873–19881.
[28] D. Liu, T.L. Kelly, Nat. Phot. 8 (2014) 133–138.
[29] H.-S. Kim, S.H. Im, N.-G. Park, J. Phys. Chem. C 118 (2014) 5615–5625.
[30] J. Qiu, Y. Qiu, K. Yan, M. Zhong, C. Mu, H. Yan, S. Yang, Nanoscale 5 (2013) 3245–3248.
[31] S. Dharani, H.K. Mulmudi, N. Yantara, P.T. Thu Trang, N.G. Park, M. Graetzel, S. Mhaisalkar, N. Mathews, P.P. Boix, Nanoscale 6 (2014) 1675–1679.
[32] M.H. Kumar, N. Yantara, S. Dharani, M. Graetzel, S. Mhaisalkar, P.P. Boix, N. Mathews, Chem. Commun. 49 (2013) 11089–11091.
[33] D. Bi, G. Boschloo, S. Schwarzmuller, L. Yang, E.M.J. Johansson, A. Hagfeldt, Nanoscale 5 (2013) 11686–11691.
[34] K. Mahmood, B.S. Swain, H.S. Jung, Nanoscale 6 (2014) 9127–9138.
[35] H.-S. Kim, J.-W. Lee, N. Yantara, P.P. Boix, S.A. Kulkarni, S. Mhaisalkar, M. Grätzel, N.-G. Park, Nano Lett. 13 (2013) 2412–2417.
[36] M. Law, L.E. Greene, J.C. Johnson, R. Saykally, P.D. Yang, Nat. Mater. 4 (2005) 455–459.
[37] D.-Y. Son, J.-H. Im, H.-S. Kim, N.-G. Park, J. Phys. Chem. C 118 (2014) 16567–16573.
[38] J. Zhang, P. Barboux, T. Pauporté, Adv. Energy Mater. 4 (2014) 1400932.
[39] D.-Y. Son, J.-H. Im, H.S. Kim, N.-G. Park, J. Phys. Chem. C 118 (2014) 16567–16573.
[40] K. Mahmood, B.S. Swain, A. Amassian, Adv. Energy Mater. 5 (2015) 1500568.
[41] J. Yang, B.D. Siempelkamp, E. Mosconi, F. De Angelis, T.L. Kelly, Chem. Mat. 27 (2015) 4229–4236.
[42] Y. Cheng, Q.-D. Yang, J. Xiao, Q. Xue, H.-W. Li, Z. Guan, H.-L. Yip, S.-W. Tsang, ACS Appl. Mater. interfaces. 7 (2015) 19986–19993.
[43] L. Zuo, Z. Gu, T. Ye, W. Fu, G. Wu, H. Li, H. Chen, J. Am. Chem. Soc. 137 (2015) 2674–2679.
[44] J. Dong, Y. Zhao, J. Shi, H. Wei, J. Xiao, X. Xu, J. Luo, J. Xu, D. Li, Y. Luo, Q. Meng, Chem. Commun. 50 (2014) 13381–13384.
[45] J. Zhao, P. Wang, L. Wei, Z. Liu, J. Zhang, H. Si, Y. Mai, X. Fang, X. Liu, D. Ren, Dalton Trans. 44 (2015) 12516–12521.
[46] M. Gratzel, Nature 414 (2001) 338–344.
[47] H.J. Snaith, C. Ducati, Nano Lett. 10 (2010) 1259–1265.
[48] P. Tiwana, P. Docampo, M.B. Johnston, H.J. Snaith, L.M. Herz, ACS Nano 5 (2011) 5158–5166.
[49] G.S. Han, H.S. Chung, D.H. Kim, B.J. Kim, J.-W. Lee, N.-G. Park, I.S. Cho, J.-K. Lee, S. Lee, H.S. Jung, Nanoscale 7 (2015) 15284–15290.
[50] Y. Li, J. Zhu, Y. Huang, F. Liu, M. Lv, S. Chen, L. Hu, J. Tang, J. Yao, S. Dai, RSC Adv. 5 (2015) 28424–28429.
[51] Z. Zhu, X. Zheng, Y. Bai, T. Zhang, Z. Wang, S. Xiao, S. Yang, Phys. Chem. Chem. Phys. 17 (2015) 18265–18268.
[52] J. Song, E. Zheng, J. Bian, X.-F. Wang, W. Tian, Y. Sanehira, T. Miyasaka, J. Mater. Chem. A 3 (2015) 10837–10844.
[53] W. Ke, G. Fang, Q. Liu, L. Xiong, P. Qin, H. Tao, J. Wang, H. Lei, B. Li, J. Wan, G. Yang, Y. Yan, J. Am. Chem. Soc. 137 (2015) 6730–6733.
[54] W. Ke, D. Zhao, A.J. Cimaroli, C.R. Grice, P. Qin, Q. Liu, L. Xiong, Y. Yan, G. Fang, J. Mater. Chem. A 3 (2015) 24163–24168.
[55] Q. Dong, Y. Shi, K. Wang, Y. Li, S. Wang, H. Zhang, Y. Xing, Y. Du, X. Bai, T. Ma, J. Phys. Chem. C 119 (2015) 10212–10217.
[56] G. Sadoughi, V. Sivaram, R. Gunning, P. Docampo, I. Bruder, N. Pschirer,

A. Irajizad, H.J. Snaith, Phys. Chem. Chem. Phys. 15 (2013) 2075–2080.
[57] L. Kranz, A. Abate, T. Feurer, F. Fu, E. Avancini, J. Löckinger, P. Reinhard, S.M. Zakeeruddin, M. Grätzel, S. Buecheler, A.N. Tiwari, J. Phys. Chem. L 6 (2015) 2676–2681.
[58] G.A.H. Wetzelaer, M. Kuik, M. Lenes, P.W.M. Blom, Appl. Phys. Lett. 99 (2011) 153506.
[59] Z. Zhu, Y. Bai, X. Liu, C.-C. Chueh, S. Yang, A.K.Y. Jen, Adv. Mater. 28 (2016) 6478–6484, http://dx.doi.org/10.1002/adma.201600619.
[60] B. Bob, T.-B. Song, C.-C. Chen, Z. Xu, Y. Yang, Chem. Mat. 25 (2013) 4725–4730.
[61] Q. Hu, J. Wu, C. Jiang, T. Liu, X. Que, R. Zhu, Q. Gong, ACS Nano 8 (2014) 10161–10167.
[62] Q. Chen, H. Zhou, Z. Hong, S. Luo, H.-S. Duan, H.-H. Wang, Y. Liu, G. Li, Y. Yang, J. Am. Chem. Soc. 136 (2014) 622–625.
[63] X. Zhao, H. Shen, Y. Zhang, X. Li, X. Zhao, M. Tai, J. Li, J. Li, H. Lin, ACS Appl. Mater. Interfaces 8 (2016) 7826–7833.
[64] X. Zhao, W. Hong, Z. Suo, Phys. Rev. B 76 (2007) 134113.
[65] K.H. Bevan, W. Zhu, H. Guo, Z. Zhang, Appl. Phys. Lett. 106 (2011) 156404.
[66] Q. Liu, M.-C. Qin, W.-J. Ke, X.-L. Zheng, Z. Chen, P.-L. Qin, L.-B. Xiong, H.-W. Lei, J.-W. Wan, J. Wen, G. Yang, J.-J. Ma, Z.-Y. Zhang, G.-J. Fang, Adv. Funct. Mater. 26 (2016) 6069–6075, http://dx.doi.org/10.1002/adfm.201600910.
[67] J.P. Correa Baena, L. Steier, W. Tress, M. Saliba, S. Neutzner, T. Matsui, F. Giordano, T.J. Jacobsson, A.R. Srimath Kandada, S.M. Zakeeruddin, A. Petrozza, A. Abate, M.K. Nazeeruddin, M. Gratzel, A. Hagfeldt, Energy Environ. Sci. 8 (2015) 2928–2934.
[68] H.J. Snaith, A. Abate, J.M. Ball, G.E. Eperon, T. Leijtens, N.K. Noel, S.D. Stranks, J.T.-W. Wang, K. Wojciechowski, W. Zhang, J. Phys. Chem. L 5 (2014) 1511–1515.
[69] T. Leijtens, E.T. Hoke, G. Grancini, D.J. Slotcavage, G.E. Eperon, J.M. Ball, M. De Bastiani, A.R. Bowring, N. Martino, K. Wojciechowski, M.D. McGehee, H.J. Snaith, A. Petrozza, Adv. Energy Mater. 5 (2015) 201500962.
[70] C.G. Van de Walle, Phys. Rev. Lett. 85 (2000) 1012–1015.
[71] G. Xiong, U. Pal, J.G. Serrano, J. Appl. Phys. 101 (2007) 024317.
[72] J. Song, E. Zheng, X.-F. Wang, W. Tian, T. Miyasaka, Sol. Energy Mater. Sol. Cells 144 (2016) 623–630.
[73] K. Nakamoto, Infrared and Raman Spectra Part a and Part B Six Edition, John Wiley & Sons, Inc., Hoboken, New Jersey, 2009, pp. 60–62.
[74] J.H. Heo, D.H. Song, H.J. Han, S.Y. Kim, J.H. Kim, D. Kim, H.W. Shin, T.K. Ahn, C. Wolf, T.-W. Lee, S.H. Im, Adv. Mater. 27 (2015) 3424–3430.
[75] S. van Reenen, M. Kemerink, H.J. Snaith, J. Phys. Chem. L (2015) 3808–3814.